

1 **Singular spectrum and principal component analysis of soil radon**
2 **(Rn-222) emanation for better detection and correlation of seismic**
3 **induced anomalies**

4 Timangshu Chetia^{1,2}, Saurabh Baruah¹, Chandan Dey^{1,2}, Sangeeta Sharma¹, Santanu Baruah¹

5 ¹Geoscience & Technology Division, CSIR-North East Institute of Science and Technology
6 (CSIR-NEIST), Jorhat-785006, Assam, India

7 ²Academy of Scientific and Innovative Research (CSIR-NEIST), Jorhat-785006, Assam, India

8 *Correspondence to: Santanu Baruah (santanub27@gmail.com)

9

10 **Abstract.** In the recent years there are several reporting's of anomalous seismic induced
11 temporal changes in soil radon emanation. It is however well known that radon anomalies apart
12 from seismic activity are also governed and controlled by meteorological parameters. This is
13 the major complication which arise for isolating the seismic induced precursory signals. Here
14 in the investigation the soil radon emanations temporal variability at Multiparametric
15 Geophysical Observatory (MPGO), Tezpur, is scrutinized in the lime light of singular spectrum
16 analysis (SSA). Further prior applying SSA Digital filter (Butterworth low pass) is applied to
17 remove the high frequen.o9cy quasi periodic component in the time series of soil radon
18 emanation. It was scrutinized that sum of just 9 eigenfunctions were sufficient enough for
19 reproducing the prominent characteristics of the overall variation. This perhaps also evinces
20 that more significantly produced fluctuations are mostly free from natural variations. The
21 variations in soil temperature was observed to be dominated by daily variations similar to radon
22 variation which account to 97.99 % whereas soil pressure accounts for 100 % of the total
23 variance which suggests that daily variations of soil radon (Rn-222) emanation are controlled
24 by soil pressure in MPGO, Tezpur during the investigation period followed by soil temperature.
25 The study concludes that SSA eliminates diurnal and semidiurnal components from time series
26 of soil radon emanation for better correlation of soil radon emanation with earthquakes.

27 1 **Introduction**

28 Radon (Rn-222) is a noble gas, a decay product of radium with atomic number, $Z=86$
29 and a half-life of nearly 3.8 days. Because of its short decay time, amount changes in its
30 production from the rock is quite evidenced. Ulomov and Mavashev in the year 1971 (Ulomov
31 and Mavashev, 1971) first suggested the correlation of radon concentration with earthquakes.
32 It has been scrutinized that the radon concentration has correlation to earthquakes and volcanic
33 eruptions (Walia et al., 2005; Singh et al., 2010; Chetia et al., 2019). Significant radon
34 concentration anomalies were also observed prior to the Uttarkashi earthquake of 20th October,
35 1991; $m_b \sim 6.5$ (Virk and Singh, 1994). Radon concentrations was monitored in the North West
36 Himalaya for earthquake prediction studies and empirical equation between earthquake
37 magnitude, epicentral distance and precursory time were examined (Choubey et al. 2009).
38 Earthquake prediction depending entirely on precursory phenomena is empirical and comprises
39 many applied problems. Among various geophysical parameters soil radon is preferred and
40 used for earthquake precursory studies because of its ease of detectability. Radon in nature has
41 different isotopes: Rn-222 (half-life~3.8 days), Rn-220 (Thoron, half-life~54.5 s) and Rn-219
42 (half-life~3.92 s). The utmost prominent is Rn-222 because of its longer half-life which is a
43 product of Ra-226 decay process. The Rn-222 emanates from soil or crust either by diffusion
44 or convection and reaches the atmosphere. The soil radon emanation concentration is generally
45 assigned to developments of micro-cracks, fissure and fracture due to dilatancy prior to
46 earthquake. This process enhances the transportation of Radon from its original enclosure
47 following the cracks into the atmosphere. Variations of soil radon and thoron concentrations
48 were also observed in fault zone prior to earthquakes SW Taiwan. Anomalous peaks were
49 discernible usually few days or weeks prior to the earthquakes (Yang et al., 2005).

50 North-East India (NE India) is highly vulnerable to earthquake and lies in seismic zone
51 V (BIS 2002) and frequent occurrence of earthquake facilitates the probability of finding

52 precursory phenomena which may lead to a successful prediction in near future. The estimated
53 cumulative probabilities show about a similar recurrence period of about 15-25 years from the
54 occurrence of last earthquake for a forecast of large earthquakes ($M_w > 5$) in the NE-India
55 region and its vicinity (Chetia et al., 2019). With this objective a Multiparametric Geophysical
56 Observatory (MPGO) in Ouguri Hills (Latitude $N26.61^\circ$; Longitude $E92.78^\circ$, Elevation~82m),
57 Tezpur, Assam, India with the installation of several geophysical instruments collecting data
58 simultaneously, portray an opportunity towards identification of precursory signatures prior to
59 earthquakes. Earthquake precursory and prediction studies advanced in late 1970s and
60 Heicheng earthquake of 4th February is a land- mark which was in short-term successfully
61 predicted in 1975 in China (Adams, 1976). The accomplished medium term forecast of $M \sim 7.5$
62 earthquake on 6th August, 1988 in northeast Indian region (Gupta, 1988) encouraged to
63 strengthen such studies in India. Another successful short term prediction was done of ($M \geq 4$)
64 in Koyana region of western India, famous for Reservoir Triggered Seismicity (Verma and
65 Bansal, 2012).

66 The study tries to correlate radon emanation in soil gas with earthquakes within the
67 epicentral distance of 100 km of $m_b > 3.1$ from MPGO, Tezpur which is situated in a highly
68 tectonically strained and seismically active region. The reason for considering the criteria of
69 100 km with $m_b > 3.1$ is the tectonic setting of the study area which is bounded by two major
70 fault namely Kopili and the Bomdila Faults. The region is highly stressed because of
71 geotectonic settings where earthquake do occur periodically within very short span of time.
72 Kopili fault zone is experiencing compressional stress due to the Indo-Burma arc and Himalyan
73 arc to the east and the north respectively which is characterized by transverse tectonics. The
74 Bomdila Fault inter-weaves across three major tectonic domains of the NE-India, namely
75 MCT, MBT and Naga-Disang thrust along NW-SE direction. (Kayal, 2010). The empirical
76 relation for the energy release E to the magnitude (Gutenberg, 1956) gives $E > 10^{9.2}$ for

77 earthquake of $m_b > 3.1$. Stress and strain are directly proportional and hence in order to obtain
78 adequate stress build up processes for observing precursory signals in temporal soil Radon
79 emanation the criteria of 100 Km with $m_b > 3.1$ is taken into consideration. The major problem
80 is the removal of quasi periodic, diurnal (mostly due to temperature) and semidiurnal (mostly
81 due to pressure) components (Kumar et al., 2015). Radon anomalies are governed by seismic
82 activity as well as by meteorological parameters (soil temperature, pressure, rainfall, moisture
83 and even wind for atmospheric radon (Stranden et al., 1984; Choubey et al., 2009; Walia et al.,
84 2005) which in turn makes it more complex for identifying the seismic induced anomalies.
85 Here in the investigation characteristics features of temporal soil radon concentrations
86 variability at MPMGO, Tezpur is scrutinized by applying singular spectrum analysis (SSA) in
87 concern to the objective of filtering the meteorological parameters on radon concentration. SSA
88 is a relatively innovative and powerful advanced method which has been used across many
89 applied problems for different scientific fields (e.g. Fraedrich, 1986; Serita et al., 2005).
90 Seismic induced emanation of soil gas radon is a complex phenomenon to be studied based on
91 mathematical, statistical analysis and modellings. Nonlinear methods such as power spectrum,
92 fractal-multifractal analysis and singular spectrum analysis etc. probably are commanding tools
93 which reveals the nonlinear features and mechanism of soil gas radon emanation processes.
94 The major advantages of Caterpillar-SSA method is that it does not require better
95 understanding of time series parametric model and extensively applicable to varied spectrum
96 of diverse temporal data. It can also be applied to match with non-stationary temporal data and
97 also permits to estimate structures even for short temporal data. Here Caterpillar-SSA method
98 is used to study the temporal soil gas radon and the foremost concept of SSA is applying PCA
99 on trajectory matrix acquired from the original time series following time series reconstruction.

100 2 Seismotectonics of the region

101 In middle of the active Kopili and Bomdila fault, the MPGO is situated. The Kopili
102 and Bomdila faults comprise Neogene-Quaternary sediments, which directly were deposited
103 over the Archean basement. The Kopili fault zone in an approx is 100 km in width and 300 km
104 in length. It is a NW-SE trending strike-slip fault (Kayal et al., 2006, Bhattacharya et al., 2008,
105 2010). The two Precambrian massifs - the Shillong Plateau and the Mikir Hills is delineated by
106 the tectonic disposition of the Kopili fault. MPGO is bounded to the north by the Main
107 Boundary Thrust (MBT) and to the south by the NE-SW trending Belt of Schuppen (Figure 1).
108 The Bomdila fault is strike slip fault of about 400 km in length which trends along WNW-ESE
109 direction. The northern portion of the fault mostly lies in the Gondwana, Paleogene and
110 Neogene sediments. This fault is surrounded by the Belt of Schuppen to the east and south by
111 the Mikir massif and to the west. The fault cuts across the Himalayan fold belt towards the
112 north (Nandy and Dasgupta, 1991).

113 The Kopili Fault has produced two large earthquakes (Figure 1) $M_w \sim 7.7$, 1869 event
114 (Figure 1) in the south eastern edge of the fault contravening the Naga-Disang thrust and
115 $M_w \sim 7.2$, 1943 earthquake which occurred farther to the north of 1869 event within a period of
116 nearly 75 years (Kayal, 2008). It is highly active with strong seismicity discernible down up to
117 depth of about 50 km, and which extends to the Main Central Thrust (MCT) in the Bhutan
118 Himalaya. Even if MCT is dormant (Ni and Barazangi, 1984), intense activity is observed at
119 the region where Kopili Fault meets the MBT and MCT (Nandy, 2001; Kayal et al., 2010,
120 2012). This is demonstrated by the August 19, 2009 Earthquake ($M_w \sim 5.1$) in the Assam Valley
121 that occurred in the center of the Kopili fault zone and the September 21, 2009 strong Bhutan
122 Himalaya earthquake ($M_w \sim 6.3$) that occurred at the northern end of the Kopili fault where it
123 connects with the MCT (Kayal et al., 2012). Both the earthquakes are shallow focus (depth ~
124 10 km) showing right lateral strike-slip faulting (Kayal et al., 2010) which suggests that the
125 Kopili fault zone is experiencing compressional stress due to the Indo-Burma arc and Himalayan

126 arc to the east and the north respectively which is characterized by transverse tectonics. The
127 Bomdila Fault inter-weaves across three major tectonic domains of the NE-India, namely
128 MCT, MBT and Naga-Disang thrust along NW-SE direction. The earthquake events along
129 Bomdila fault occur in a diffused pattern having post-collisional intracratonic characteristics
130 (Nandy and Dasgupta, 1991). It is observed that, the Upper Brahmaputra Valley stretching
131 between the Bomdila Fault and almost near NW-trending Mishmi Thrust in the northeast is
132 seismically dormant, and is recognized as the Assam Gap (Khattri, 1983).

133 **3 Method and techniques**

134 **3.1 Soil radon (Rn-222) time series**

135 A BMC2 barasol manufactured by Algade is into operation for soil radon emanation
136 time series data in MPGO for earthquake prediction and precursory studies. Soil gas radon
137 emanation every 15 minutes is being continuously monitored. The barasol probe is kept fitted
138 inside a plastic tube (length 1.5m and diameter of 0.0635m) with open bottom dug inside the
139 ground in such a way that the detection unit (detector sensitivity-0.02 pulses/h for 1 Bq/m³ and
140 saturation volumetric activity-3MBq/ m³) which is at the bottom of the probe lies 1m from the
141 ground level. A silicon alpha detector detects the radon gas which enters the detection chamber
142 when it emanates from the soil. The radon pass in a detection volume over three cellulose filters
143 which allows to trap all the solid daughter products of radon. The sensor is a fixed silicon
144 detector with a depleted depth of 100 μ m and 400 mm² of sensitive area. It performs the
145 counting by atomic spectrometry of radon (Rn-222) and daughter products created in the
146 detection volume (with window customized between 1.5 MeV and 6 MeV). The probe system
147 is embedded with soil pressure and temperature sensor. The sensor calibration permits the
148 volumic activity of the radon (Rn-222) to be evaluated. In the present investigation the soil
149 radon emanation temporal variability at MPGO, Tezpur the radon data were prudently checked

150 for no gaps or discontinuous jump. Digital filter (Butterworth) is applied to eliminate the high
 151 frequency quasi periodic components from the soil radon time series for better discernibility of
 152 seismic induced anomalies.

153 3.2 Singular Spectrum Analysis

154 The SSA results and graphs in the investigation are acquired by using Caterpillar-SSA
 155 3.40 software (Alexandrov and Golyandina, 2004). Window selection rule applied to the time
 156 series is one half of the length of the time series to meet the theoretical requirements for the
 157 investigation (Golyandina, 2010, Khan, 2011, Hassani, 2007). The singular value
 158 decomposition (SVD) algorithm was applied as it is more accurate than QR iteration which
 159 are the most common algorithm for solving of eigenvalues and singular value problems
 160 (Demmel and Veselić, 1992). The main objective of SSA is decomposing the original time
 161 series into sum of series such that each of the component in this sum can be known (either as a
 162 trend, periodic or quasi-periodic components) or noise. This is accomplished by decomposition
 163 and reconstruction. At the first the time series is decomposed following the reconstruction of
 164 the original time series (which is without noise). The methodology adopted here is first to
 165 embedding a 1-dimension time series say, $Y_T = (y_1, \dots, y_T)$ into a multi-dimensional time series
 166 X_1, \dots, X_K having vectors $X_i = (y_i, \dots, y_{i+L-1}) \in R^L$ (Golyandina et al., 2001, 2001). Here the value
 167 of $K = T - L + 1$. The X_i Vectors are called L -lagged vectors. The embedding depends on the
 168 window length L , such that $2 \leq L \leq T$ which results for trajectory matrix (Hankel matrix:
 169 diagonal elements $i + j = \text{const.}$ are equal) $X = [X_1, \dots, X_K] = (X_{ij})_{i,j=1}^{L,K}$. Secondly the Singular
 170 Value Decomposition (SVD) of the trajectory matrix is performed to represent it as an addition
 171 of bi-orthogonal elementary matrices having rank one. Represented by $\lambda_1, \dots, \lambda_L$ which are the
 172 Eigen-values of XX' in a descending order of magnitude ($\lambda_1 \geq \dots \lambda_L \geq 0$) and by U_1, \dots, U_L which
 173 are the orthonormal system (i.e. $(U_i, U_j) = 0$ for $i \neq j$) is the orthogonality property and $\|U_i\|=1$,

174 of the eigenvectors of the matrix XX' corresponding to these eigenvalues. (U_i, U_j) is the inner
 175 product of the vectors U_i and U_j and $\|U_i\|$ is the norm of the vector U_i . The Set

$$176 \quad d = \max (i, \text{ such that } \lambda_i > 0) = \text{rank } X \quad (\text{I})$$

177 If we represent $V_i = X' U_i / \sqrt{\lambda_i}$, then SVD of the trajectory matrix can be represented
 178 as:

$$179 \quad X = X_1 + \dots + X_d \quad (\text{II})$$

180 Here $X_i = \sqrt{\lambda_i} U_i V_i'$ ($i = 1, \dots, d$).

181 Thirdly the series reconstruction is accomplished by grouping, to split the elementary
 182 matrices (X_i) into various groups and addition of the matrices within each and every group. The
 183 splitting of the elementary matrices X_i into several groups and summation of the matrices
 184 within individual group is grouping. Say $I = (i_1, \dots, i_p)$ is a group of indices i_1, \dots, i_p . Now
 185 for the group I of corresponding matrix X_I is defined as $X_I = X_{i_1} + \dots + X_{i_p}$. The spiltng
 186 of the of the set with indices $J = 1, \dots, d$ on the disjoint subsets I_1, \dots, I_m resembles to the
 187 illustration

$$188 \quad X = X_{I_1} + \dots + X_{I_m}. \quad (\text{III})$$

189 This procedure of selecting the sets I_1, \dots, I_m is termed as eigentriple grouping. For given
 190 group I the contribution of the component X_I into $X_{I_1} + \dots + X_{I_m}$ is estimated to the corresponding
 191 eigenvalues as: $\sum_{i \in I} \lambda_i / \sum_{i=1}^d \lambda_i$.

192 Finally diagonally averaging transfers each I matrix into a time series, which is an
 193 additive component of the initial series Y_T . If z_{ij} is an element of the matrix Z . Then k-th term
 194 of the produced series is acquired by averaging z_{ij} for i, j such that $i + j = k + 2$. This procedure
 195 is known as diagonal averaging (Hankelization) of the matrix Z . The Hankelization of a matrix

196 Z is the Hankel matrix HZ which is the trajectory matrix corresponding to the series obtained
 197 from diagonal averaging. Hankelization is a best logical technique that HZ matrix is the nearest
 198 to Z among all corresponding size of Hankel matrices (Golyandina et al., 2001). Now applying
 199 the Hankelization technique to each and every matrix components in equation III, we get

$$200 \quad X = \tilde{X}_{I_1} + \dots + \tilde{X}_{I_m} \quad (IV)$$

201 Here $X_{I_1} = HX$ corresponding to initial series $Y_T = (y_1, \dots, y_T)$ decomposition into a
 202 sum of m series as

$$203 \quad y_t = \sum_{k=1}^m y_t^{\sim(k)} \quad (V)$$

204 Here $y_t^{\sim(k)} = y_1^{\sim(k)} + \dots + y_T^{\sim(k)}$ corresponds matrix X_{I_j} .

205 Covariance matrix is a matrix of covariances between the values $X(t)$ and $X(t+k)$., where
 206 k is a lag. When k is positive $X(t)$ and $X(t+k)$ tends to fluctuate together. The covariances among
 207 $X(t)$ and $X(t+k)$ can be estimated as

$$208 \quad COV = \frac{\sum_{i=1}^n (X(t) - \overline{x(t)})(X(t+k) - \overline{x(t+k)})}{n-1} \quad (VI)$$

209 Where $\overline{x(t)}$ and $\overline{x(t+k)}$ represents the mean of $x(t)$ and $x(t+k)$ correspondingly.

210 Now covariance matrix (\tilde{C}) can be obtained by putting equal values \tilde{c}_{ij} at each matrix
 211 antidiagona $|i-j| = k$ as

$$212 \quad \tilde{c}_{ij} = \frac{1}{N-|i-j|} \sum_{m=1}^{N-|i-j|} x_m x_{m+|i-j|} \quad (VII)$$

213 Where $1 \leq i, j \leq L$, N is the length of the time series and $|i-j| = k$.

214 From the eigenvectors of the covariance matrix measured at different lags the principal
 215 components of the time series is estimated. The principal components is also a time series

216 having same length as the “embedded” time series. The computation of principal component is
 217 from simple matrix product as

$$218 \quad \text{PC} = \tilde{C} * \text{matrix of eigenvectors} \quad (\text{VIII})$$

219 Where \tilde{C} is the covariance matrix, whose elements are \tilde{c}_{ij} .

220 The exemplification of how discretely different component can be separated from each
 221 other is based on studying the SSA properties. To successfully decompose (SSA) the series Y_T
 222 the subsequent additive components of the series should be almost separable from each other.
 223 The weighted correlation is also known as *w-correlation* which is the natural measurement of
 224 dependencies among two series Y_T^1 and Y_T^2 given as:

$$225 \quad \rho_{12}^\omega = \frac{(Y_T^1, Y_T^2)_\omega}{\|Y_T^1\|_\omega \|Y_T^2\|_\omega} \quad (\text{IX})$$

226 Here, $\|Y_T^1\|_\omega = \sqrt{(Y_T^1, Y_T^1)_\omega}$, $(Y_T^i, Y_T^j)_\omega = \sum_{k=1}^T \omega_k y_k^i y_k^j$, $(i, j = 1, 2)$, $\omega_k = \min\{k, T -$
 227 $k\}$ while assuming $L \leq T/2$.

228 If the absolute value of *w-correlations* is small, the corresponding series are almost *w-*
 229 orthogonal. On the other hand if it is large, the series are not *w-orthogonal* and are considered
 230 probably un-separable. If the reconstructed components exhibit *w-correlation* zero, it signifies
 231 the two components to be separable. Large values of *w-correlations* between reconstructed
 232 components indicate that the components should possibly be gathered into one group and
 233 correspond to the same component in SSA decomposition (Hassani, 2007).

234 **4 Results**

235 The average value of radon for a period of six month from April 2017-September 2017
 236 was found to be in the range 55-117 kBq/m³. The average emanation of soil-gas radon and the

237 standard deviation at MPMO from April to September 2017 is illustrated in Table 1.
238 Simultaneously variation of soil temperature and pressure with radon emanation was observed.
239 Usually, radon shows positive correlation with temperature i.e. the soil radon concentration
240 increases with increase in temperature and decreases as temperature decrease. The correlation
241 coefficient (Pearson correlation) between radon and temperature is found to be 0.5 signifying
242 positive correlation, while the correlation coefficient between radon and pressure is found to
243 be -0.5 signifying negative correlation with an average temperature and pressure of 28.60 °C
244 and 991.03 mbar respectively during afore mentioned period. The positive correlation of radon
245 with temperature might be due to the rise in diffusion rate with temperature (Sharma et al.
246 2000; Singh et al. 2008). The negative correlation coefficient was found for soil radon and
247 pressure which signify, with the increase in pressure, the radon emanation decreases while with
248 the decrease in pressure the radon emanation increases. In general, the negative correlation is
249 due to the diffusion process which slows down with increase in pressure, which in turn
250 decreases the radon concentration in the soil. The average value of pressure, temperature,
251 standard deviation, coefficient of variation and correlation coefficient for the observation
252 period is detailed in Table 2. The maximum and minimum temperature observed was 31.24 °C
253 and 23.78 °C i.e. a change of 7.46 °C during the period of observation. Simultaneously, the
254 maximum and minimum pressure during the period of observation was 999.32 mbar and 980.72
255 mbar i.e. a change of 18.6 mbar. Digital filter (Butterworth) is applied to eliminate the high
256 frequency quasi periodic components from the soil radon time series for better discernibility of
257 seismic induced anomalies and is represented in Figure 2.

258 The covariance matrix of the first 9 group of soil radon (Rn-222) time series is
259 represented in Figure 3. The singular value decomposition (SVD) to Rn-222 data evinced that
260 first 9 eigenfunctions (Figure 4) when grouped resulted for 99.90 % of the total variance in the
261 individual time series. The eigenfunction group 1 and 2 represents the aperiodic component and

262 group 3 to 9 represented periodic components. It has been earlier studied that the periodic
263 components of radon data extracted by SSA consisted of diurnal and semidiurnal components
264 since the components included variation of 24-hour and 12- hour period (Kumar et al., 2015).
265 The decomposed eigenvectors in soil radon time series is grouped into two classes as diurnal
266 and semidiurnal variation. The sum of eigenfunction group 1 and 2 accounts for 98.62 % and
267 group 3 to 9 accounts for 0.48 % of the variance. Radon variations is governed by daily
268 variations, which accounts to 99.90 % of the total variance in soil gas radon at the MPGO,
269 Tezpur. The Principal Component of soil radon (Rn-222) related to the first 9 grouping of
270 eigentriples is represented in Figure 5 and w-correlation matrix for the 9 reconstructed
271 components is represented in Figure 6.

272 The covariance matrix of the first 9 group of soil temperature and pressure time series
273 is represented in Figure 7 and Figure 11 respectively. The decomposed eigenfunctions for soil
274 temperature and pressure time series by applying SSA is represented in Figure 8 and Figure 12
275 respectively. The first 9 eigenfunction group from SVD to atmospheric temperature records
276 accounts nearly about 99.99 % and first 9 eigenfunction group of soil pressure 100 % of the
277 variation respectively. It is discernible that first eigenfunction 1 alone itself is capable of
278 producing 100 % variation but the time series is well modeled when first 9 eigenfunction is
279 grouped. This evinces SVD to radon, soil temperature and soil pressure data evince that first
280 9 eigenfunction accounts >98.00 % of the variance of the individual data series. This is
281 fascinating to observe that sum of first 9 eigenfunction is fairly sufficient to reproduce the
282 prominent features of the overall variation. This also suggests that the most significantly
283 produced variations are mostly free from naturally induced variations. Soil pressure variations
284 are dominated by semidiurnal variations by 100 % of the total variation in atmospheric pressure
285 at MPGO, Tezpur. On the other hand soil temperature variations is dominated by daily
286 variations like radon variation which account to 97.99 % whereas soil pressure accounts for

287 100 % of the total variance. This suggest that daily variations of soil radon (Rn-222) emanation
288 are controlled by soil pressure in MPGO, Tezpur during the investigation period followed by
289 soil temperature. The Principal Component of soil temperature related to the first 9 grouping
290 of eigentriples is represented in Figure 9 and w-correlation matrix for the 9 reconstructed
291 components is represented in Figure 10. The Principal Component of soil pressure related to
292 the first 9 grouping of eigentriples is represented in Figure 13 and w-correlation matrix for the
293 9 reconstructed components is represented in Figure 14. The reconstructed time series for soil
294 radon (Rn-222), temperature and pressure is represented is Figure 15 and it's residual in Figure
295 16. It is also discernible that the during the investigation time period the pressure change was
296 more than temperature change which also evinces the variation of soil radon at MPGO, Tezpur
297 was more governed by pressure followed by temperature change. The quasi periodic, diurnal
298 (periodic mostly due to temperature) and semidiurnal (aperiodic mostly due to pressure) were
299 eliminated by Singular Spectrum Analysis in the reconstructed time series by grouping and
300 analyzing the eigenfunctions and principle component of individual time series of Rn-222,
301 temperature and pressure respectively. The soil pressure and temperature were found to be
302 negatively correlated to each other (-0.62) which produces a pseudo effect in the soil radon
303 time series. The grouping and reconstruction of the time series also eliminates these pseudo
304 effect arising due soil pressure and temperature.

305 **5 Discussion**

306 The reconstructed soil radon time series along with the seismic activity during the
307 investigation period is shown in Figure 17. The hypocentral parameters of the earthquake
308 events found to have correlation with soil radon emanation is listed in Table 3. The earthquakes
309 are selected from a catalogue which follow Stationary Poisson process where we have adopted
310 declustering method by Reasenberg (Reasenberg, 1985). After declustering of the database, we
311 have used the maximum likelihood algorithm provided by ZMAP (Wiemer, 2001) to perform

312 a Gutenberg-Richter regression (Gutenberg and Richter, 1944). Here, the magnitude range of
313 earthquakes catalog indicate relatively high magnitude of completeness ($M_C \sim 4.7$) for the
314 region. It was observed that there were certain positive amplitude rise anomalies in radon
315 emanation prior to six out of 9 earthquakes which occurred in the vicinity (100 km radially
316 from MANGO, Tezpur). Increase in the soil radon concentration is generally assigned to
317 developments of microcracks, fractures and fissure caused by dilatancy prior to earthquake.
318 This process enhances the transportation of radon from its original enclosure following the
319 cracks. The rise in soil radon concentration prior to an earthquake may be due to the strain
320 buildup processes in the area. During this process, very small fractures are developed in the
321 rocks which enhances the contribution of radon gas to the soil near the surface of earth
322 (Miklavčić et al., 2008). Three earthquake events were preceded by negative anomalies. The
323 negative anomalies might be due to the circumstance that during the final stage of dilatancy
324 model prior to an earthquake the Rn-222 emanation can be stable or it can decrease (Tomer,
325 2016). This is because, during the final stage prior an earthquake, rupture occurs and fluid
326 pressure and stress on rocks is released (Bakhmutov and Groza, 2008). The fluid pressure
327 increases may result in water level rise (pore spaces probably gets filled by water and diffusion
328 rate of radon is more in void than in water filled pore space; Nielson et al., 1984; Merolla et
329 al., 2003) and this probably does not allow the soil gas Rn-222 to escape from the surface which
330 in turn reduces or stabilizes the emanation of Rn-222. Further a decreasing radon anomaly as
331 observed in this study may be the result of squeezing effect of compressional stress built up in
332 the rock, which in turn result in soil porosity changes at micro scale. There were certain events
333 which occurred on the same day or just a very short seismic gap of 1 or 2 days. Here in the case
334 earthquake with higher magnitude might also be the probable reason for the anomalous
335 behavior of the soil gas radon emanation, as for spatio-temporal clustered earthquakes, the
336 largest magnitude earthquake is presumed to precede the anomalies in radon emanation

337 (Hartmann and Leavy, 2005). Positive as well as negative anomalies were observed prior to 9
338 events which occurred in the vicinity (100 km radially from MPGO) with in a short span of
339 time.

340 **6 Conclusion**

341 The investigation concludes that digital filter assists in eliminating the high frequency
342 quasi periodic components from the time series. The SSA method helps eliminating the diurnal
343 and semidiurnal fluctuations from soil radon time series for improved correlating and detection
344 of the soil radon emanation with seismic activity. The investigation also evinced that radon is
345 dominated by daily variation at MPGO, Tezpur and is controlled by soil pressure followed by
346 temperature. It is also concluded that principle component analysis helps in removing the
347 pseudo effect pertaining to simultaneous soil pressure and temperature effect. It was observed
348 that there were certain positive amplitude rise anomalies in radon emanation prior to six events
349 out of 9 earthquakes which occurred in the vicinity (100 km radially from MPGO, Tezpur)
350 within a short span of time. The increase of radon emanation with temperature might be the
351 result of increasing diffusion rate with temperature. Three earthquake events were preceded by
352 negative anomalies. The negative anomalies might be due to the circumstance that during the
353 final stage of dilatency model prior to an earthquake the soil gas radon emanation can be stable
354 or it can decrease. This is because, during the final stage prior an earthquake, rupture occurs
355 and fluid pressure and stress on rocks is released. Further a decreasing radon anomaly as
356 observed in this study may be the result of squeezing effect of compressional stress built up in
357 rock, which in turn changes porosity of soil at micro scale.

358 **Acknowledgements.** We acknowledge our sincere thanks to Ministry of Earth Sciences
359 (MoES) Government of India for providing funds vide project no. MoES/P.O.(Seismo)/NPEP-
360 16/2011. We thank Director, CSIR-NEIST Jorhat for giving necessary permission to publish
361 this paper.

362 **References**

- 363 Adams, R. D.: The Haicheng, China, earthquake of 4 February 1975; the first successfully
 364 predicted major earthquake, *Earthquake Engineering & Structural Dynamics*, 4, 423-
 365 437, 1976.
- 366 Alexandrov, T., and Golyandina, N.: The automatic extraction of time series trend and
 367 periodical components with the help of the Caterpillar-SSA approach, *Exponenta Pro*,
 368 3, 54-61, 2004.
- 369 Bakhmutov, V., and Groza, A.: The dilatancy-diffusion model: new prospects, *Proceedings*,
 370 *International Conference: Problems of Geocosmos*, 7th, St. Petersburg, Russia, May,
 371 2008, 26-30.
- 372 Bhattacharya, P. M., Mukhopadhyay, S., Majumdar, R., and Kayal, J.: 3-D seismic structure
 373 of the northeast India region and its implications for local and regional tectonics,
 374 *Journal of Asian Earth Sciences*, 33, 25-41, 2008.
- 375 Bhattacharya, P. M., Kayal, J., Baruah, S., and Arefiev, S.: Earthquake source zones in
 376 northeast India: seismic tomography, fractal dimension and b value mapping, in:
 377 *Seismogenesis and Earthquake Forecasting: The Frank Evison Volume II*, Springer,
 378 145-158, 2010.
- 379 Chetia, T., Baruah, S., Dey, C., Sharma, S., and Baruah, S.: Multi-parametric approach for
 380 Earthquake Precursor Detection in Assam Valley (Eastern Himalaya, India) using
 381 Satellite and Ground Observation Data, *Geotectonics*, In Press, 2019.
- 382 Chetia, T., Baruah, S., Dey, C., Sharma, S., and Baruah, S.: Probabilistic analysis of seismic
 383 data for earthquake forecast in North-East India and its vicinity, *Current Science*, In
 384 Press, 2019.
- 385 Choubey, V., Kumar, N., and Arora, B.: Precursory signatures in the radon and geohydrological
 386 borehole data for M4. 9 Kharsali earthquake of Garhwal Himalaya, *Science of the total*
 387 *environment*, 407, 5877-5883, 2009.
- 388 Demmel, J., and Veselić, K.: Jacobi's method is more accurate than QR, *SIAM Journal on*
 389 *Matrix Analysis and Applications*, 13, 1204-1245, 1992.
- 390 Fraedrich, K.: Estimating the dimensions of weather and climate attractors, *Journal of the*
 391 *atmospheric sciences*, 43, 419-432, 1986.
- 392 Golyandina, N., Nekrutkin, V., and Solntsev, V.: „Caterpillar“-SSA Technique for Analysis of
 393 Time Series in Economics, *New Models of Business: Managerial Aspects and Enabling*
 394 *Technology*, 198, 2001.
- 395 Golyandina, N., Nekrutkin, V., and Zhigljavsky, A. A.: *Analysis of time series structure: SSA*
 396 *and related techniques*, Chapman and Hall/CRC, 2001.
- 397 Golyandina, N.: On the choice of parameters in singular spectrum analysis and related
 398 subspace-based methods, arXiv preprint arXiv:1005.4374, 2010.
- 399 Gupta, H.: Medium-term earthquake prediction, *Eos, Transactions American Geophysical*
 400 *Union*, 69, 1620-1630, 1988.

REVISED VERSION

- 401 Gutenberg, B., and Richter, C. F.: Frequency of earthquakes in California, Bulletin of the
402 Seismological society of America, 34, 185-188, 1944.
- 403 Gutenberg, B.: The energy of earthquakes, Quarterly Journal of the Geological Society, 112,
404 1-14, 1956.
- 405 Hartmann, J., and Levy, J. K.: Hydrogeological and gasgeochemical earthquake precursors—A
406 review for application, Natural Hazards, 34, 279-304, 2005.
- 407 Hassani, H.: Singular spectrum analysis: methodology and comparison, 2007.
- 408 Kayal, J., Arefiev, S., Barua, S., Hazarika, D., Gogoi, N., Kumar, A., Chowdhury, S., and
409 Kalita, S.: Shillong plateau earthquakes in northeast India region: complex tectonic
410 model, CURRENT SCIENCE-BANGALORE-, 91, 109, 2006.
- 411 Kayal, J.: Microearthquake seismology and seismotectonics of South Asia, Springer Science
412 & Business Media, 2008.
- 413 Kayal, J., Arefiev, S. S., Baruah, S., Tatevossian, R., Gogoi, N., Sanoujam, M., Gautam, J.,
414 Hazarika, D., and Borah, D.: The 2009 Bhutan and Assam felt earthquakes (Mw 6.3
415 and 5.1) at the Kopili fault in the northeast Himalaya region, Geomatics, Natural
416 Hazards and Risk, 1, 273-281, 2010.
- 417 Kayal, J., Arefiev, S., Baruah, S., Hazarika, D., Gogoi, N., Gautam, J., Baruah, S., Dorbath, C.,
418 and Tatevossian, R.: Large and great earthquakes in the Shillong plateau—Assam valley
419 area of Northeast India Region: Pop-up and transverse tectonics, Tectonophysics, 532,
420 186-192, 2012.
- 421 Khan, M. A. R., and Poskitt, D.: Window length selection and signal-noise separation and
422 reconstruction in singular spectrum analysis, Monash Econometrics and Business
423 Statistics Working Papers, 23, 2011-2023, 2011.
- 424 Khattri, K., and Tyagi, A.: Seismicity patterns in the Himalayan plate boundary and
425 identification of the areas of high seismic potential, Tectonophysics, 96, 281-297, 1983.
- 426 Kumar, A., Walia, V., Arora, B. R., Yang, T. F., Lin, S.-J., Fu, C.-C., Chen, C.-H., and Wen,
427 K.-L.: Identifications and removal of diurnal and semidiurnal variations in radon time
428 series data of Hsinhua monitoring station in SW Taiwan using singular spectrum
429 analysis, Natural Hazards, 79, 317-330, 2015.
- 430 Merolla, P., Mose, D., and King, A.: Effect of water table fluctuations on radon emanation
431 from soil, 2003.
- 432 Miklavčić, I., Radolić, V., Vuković, B., Poje, M., Varga, M., Stanić, D., and Planinić, J.: Radon
433 anomaly in soil gas as an earthquake precursor, Applied radiation and isotopes, 66,
434 1459-1466, 2008.
- 435 Nandy, D., and Dasgupta, S.: Seismotectonic domains of northeastern India and adjacent areas,
436 Physics and Chemistry of the Earth, 18, 371-384, 1991.
- 437 Nandy, D.: Geodynamics of Northeastern India and the adjoining region, ACB publications,
438 2001.

REVISED VERSION

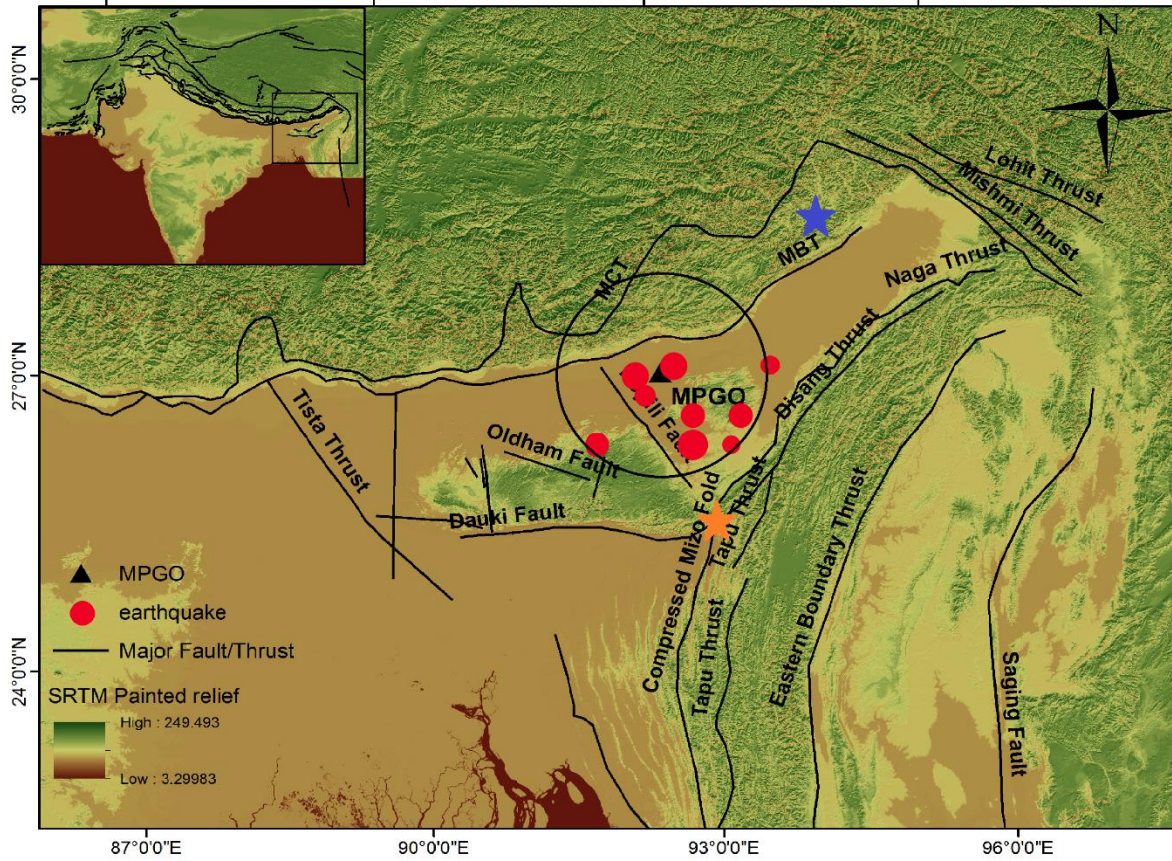
- 439 Ni, J., and Barazangi, M.: Seismotectonics of the Himalayan collision zone: Geometry of the
440 underthrusting Indian plate beneath the Himalaya, *Journal of Geophysical Research:*
441 *Solid Earth*, 89, 1147-1163, 1984.
- 442 Nielson, K., Rogers, V., and Gee, G.: Diffusion of Radon through Soils: A Pore Distribution
443 Model 1, *Soil Science Society of America Journal*, 48, 482-487, 1984.
- 444 Reasenberg, P.: Second-order moment of central California seismicity, 1969–1982, *Journal of*
445 *Geophysical Research: Solid Earth*, 90, 5479-5495, 1985.
- 446 Serita, A., Hattori, K., Yoshino, C., Hayakawa, M., and Isezaki, N.: Principal component
447 analysis and singular spectrum analysis of ULF geomagnetic data associated with
448 earthquakes, *Natural Hazards and Earth System Science*, 5, 685-689, 2005.
- 449 Sharma, A. K., Walia, V., and Virk, H.: Effect of meteorological parameters on radon
450 emanation at Palampur (HP), *Journal of Association of Exploration Geophysicists*, 21,
451 47-50, 2000.
- 452 Singh, S., Kumar, A., Bajwa, B. S., Mahajan, S., Kumar, V., and Dhar, S.: Radon monitoring
453 in soil gas and ground water for earthquake prediction studies in North West Himalayas,
454 *India, Terr. Atmos. Ocean. Sci*, 21, 685-695, 2010.
- 455 Stranden, E., Kolstad, A., and Lind, B.: The influence of moisture and temperature on radon
456 exhalation, *Radiation Protection Dosimetry*, 7, 55-58, 1984.
- 457 Tomer, A.: Radon as a earthquake precursor: a review, *Int J Sci Eng Technol*, 4, 815-822, 2016.
- 458 Ulomov, V., and Mavashev, B.: *The Tashkent Earthquake of 26 April*, Tashkent: Acad. Nauk.
459 *Uzbeck*, 1971.
- 460 Verma, M., and Bansal, B. K.: Earthquake precursory studies in India: Scenario and future
461 perspectives, *Journal of Asian Earth Sciences*, 54, 1-8, 2012.
- 462 Virk, H., and Singh, B.: Radon recording of Uttarkashi earthquake, *Geophysical Research*
463 *Letters*, 21, 737-740, 1994.
- 464 Walia, V., Su, T., Fu, C., and Yang, T.: Spatial variations of radon and helium concentrations
465 in soil-gas across the Shan-Chiao fault, Northern Taiwan, *Radiation Measurements*, 40,
466 513-516, 2005.
- 467 Wiemer, S.: A software package to analyze seismicity: ZMAP, *Seismological Research Letters*,
468 72, 373-382, 2001.
- 469 Yang, T., Walia, V., Chyi, L., Fu, C., Chen, C.-H., Liu, T., Song, S., Lee, C., and Lee, M.:
470 Variations of soil radon and thoron concentrations in a fault zone and prospective
471 earthquakes in SW Taiwan, *Radiation Measurements*, 40, 496-502, 2005.
- 472
- 473
- 474
- 475

476 **FIGURES AND TABLES**

477

478

479



480

481 **Figure 1:** Map illustrates the main tectonic features of North-East (after Kayal, 2006), India

482 along with the study area represented by black color circle and the earthquake events ($3.1 \geq mb$

483 ≤ 3.7) which were found to have correlation with soil radon emanation anomalies are

484 represented by the red color dots. The black color triangle represents the Multiparametric

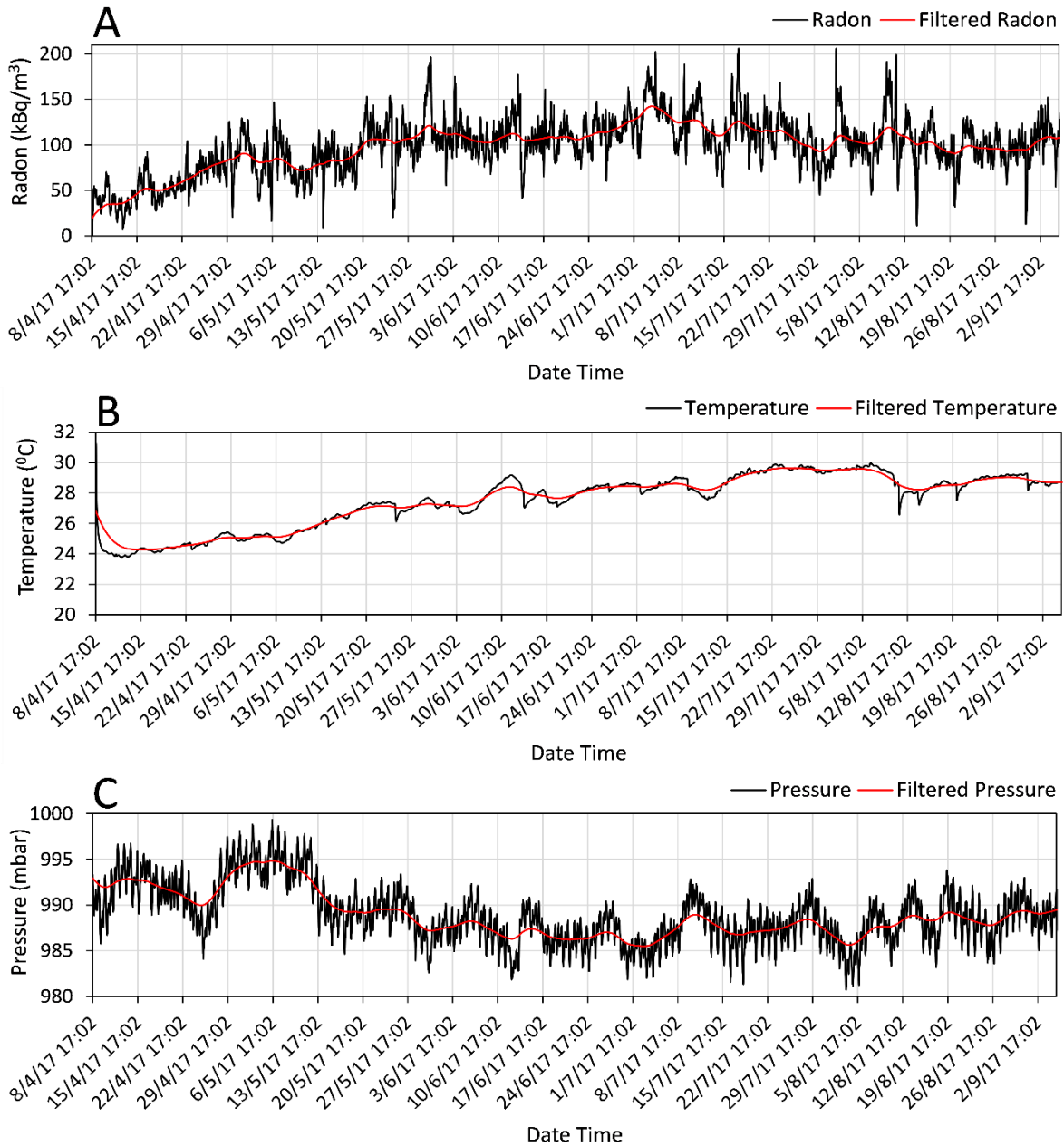
485 Geophysical Observatory. The blue color star represents the earthquake of $M_w \sim 7.2$, 1947 and

486 orange color star represents the earthquake of $M_w \sim 7.7$, 1869.

487

488

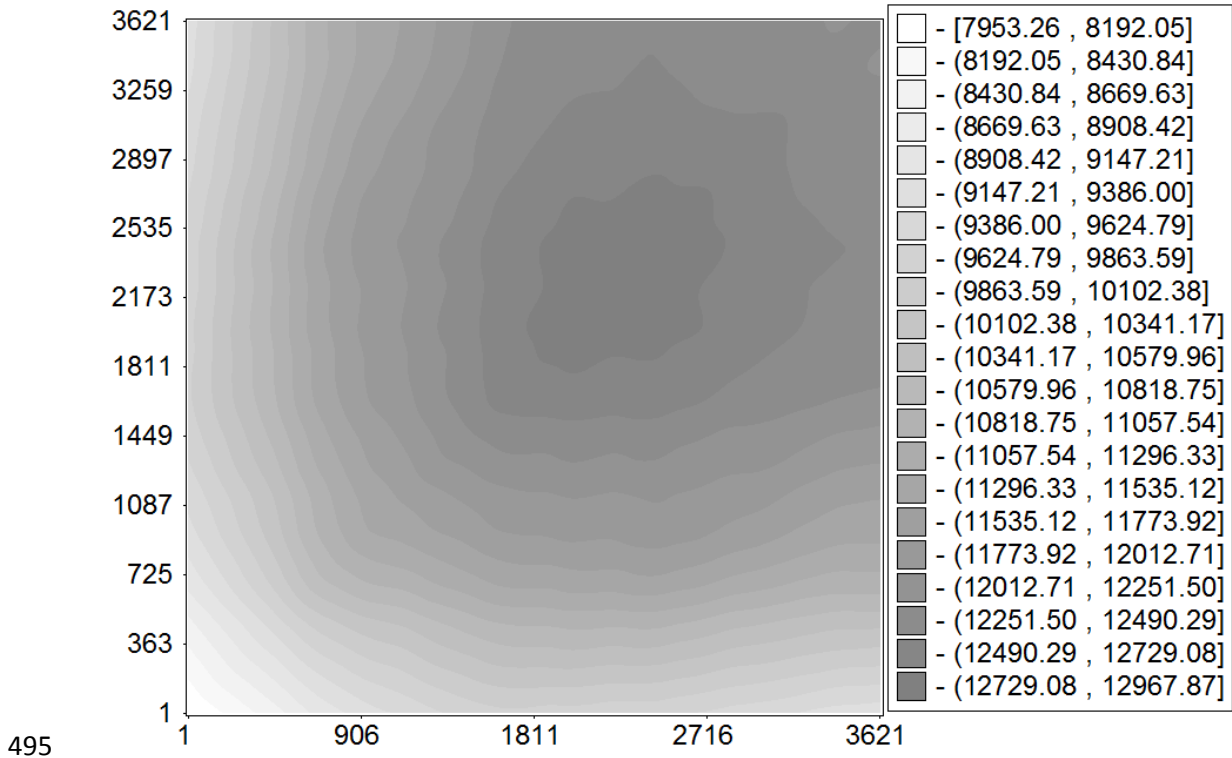
489



490

491 **Figure 2:** The plot represents the removal of high frequency quasi periodic component for A)
 492 filtered time series of soil radon, B) filtered time series of soil temperature and C) filtered time
 493 series of soil pressure.

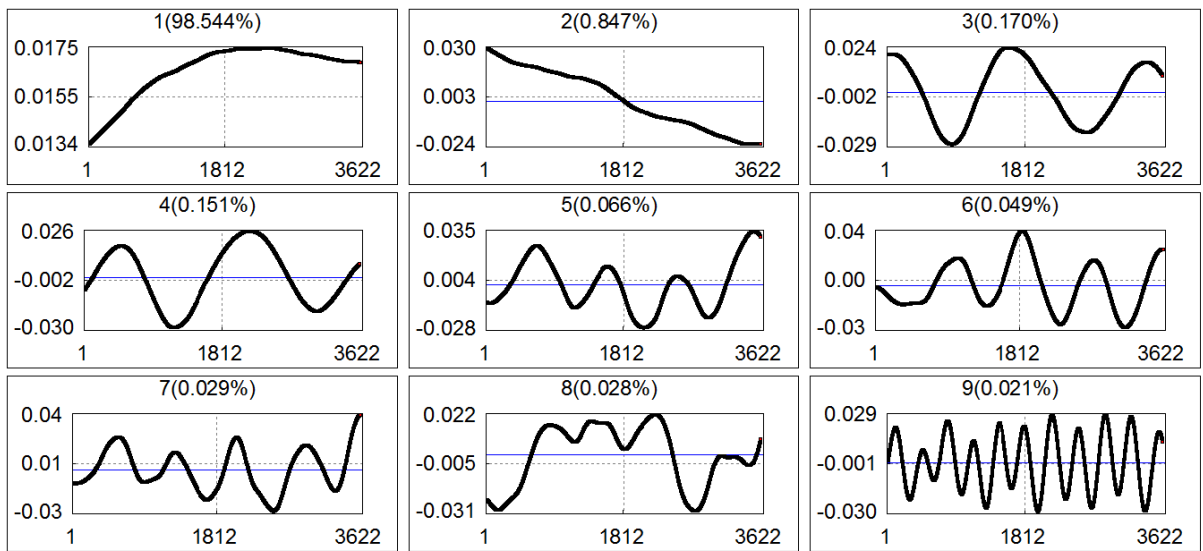
494



495

496 **Figure 3:** Covariance matrix of the first 9 group of soil radon (Rn-222) time series.

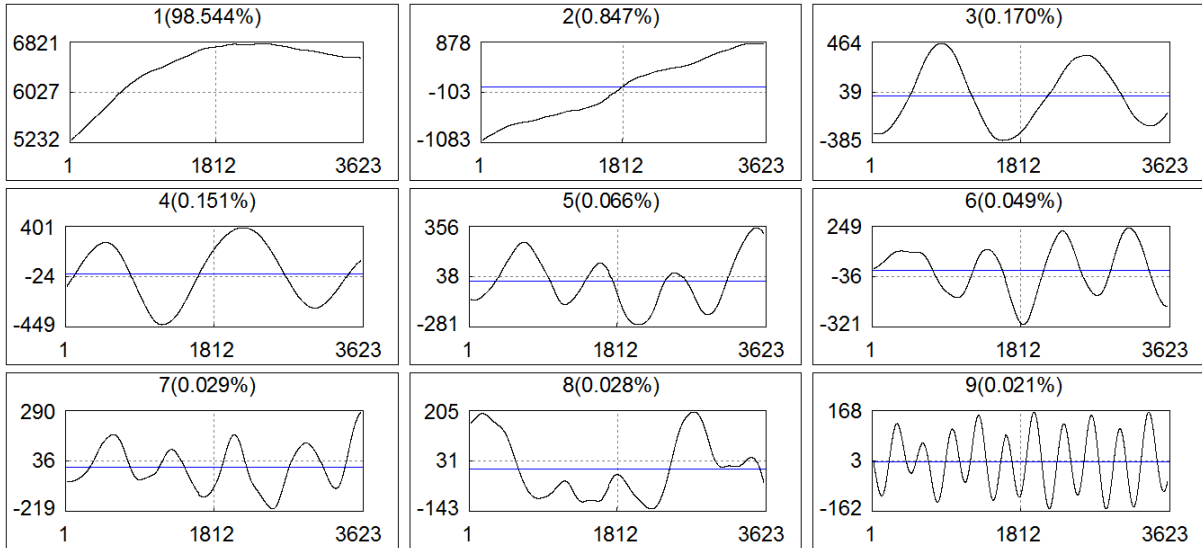
497



498

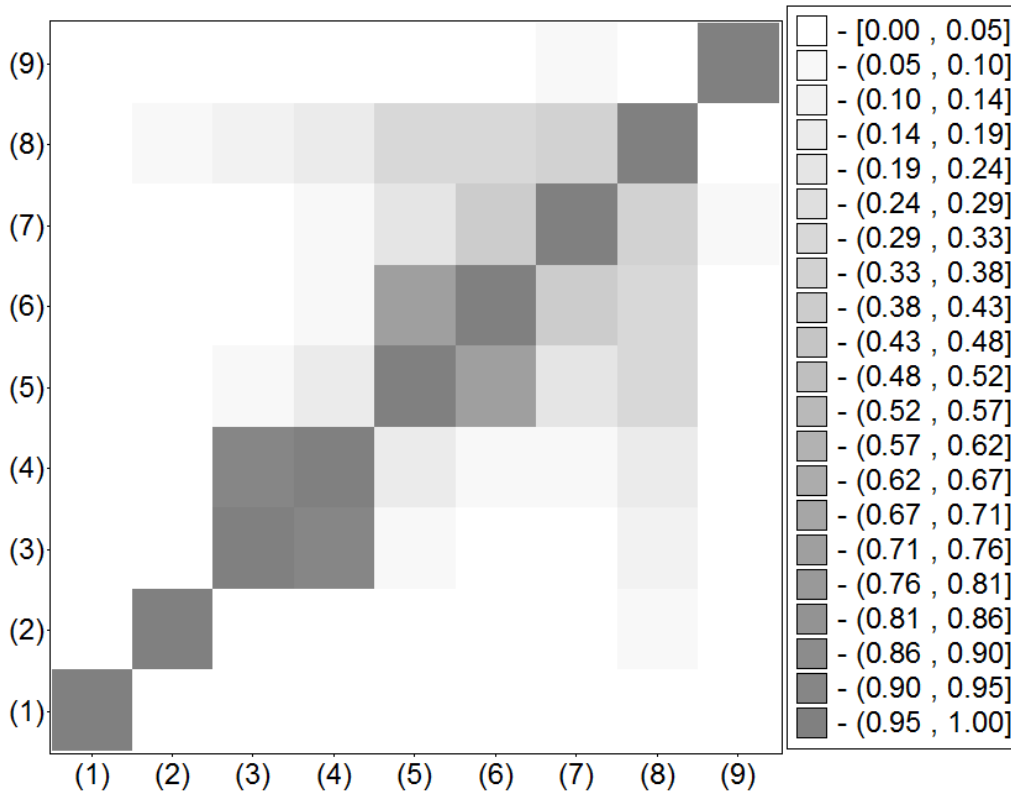
499 **Figure 4:** Eigenfunctions of soil radon (Rn-222) first 9 group. The scale in the horizontal x-
 500 axis represents the window length ($L*15$ minutes) and the scale in the vertical y-axis represents
 501 the singular eigenvectors (matrix path SVD).

REVISED VERSION



502

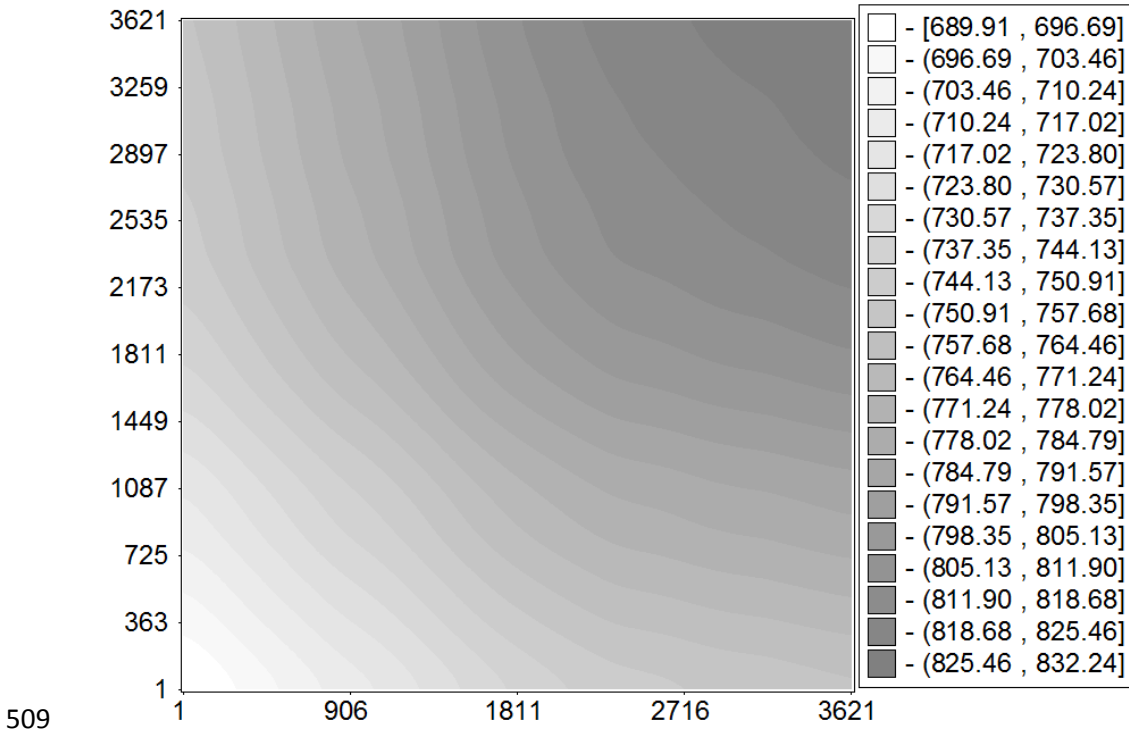
503 **Figure 5:** Principal Component of soil radon (Rn-222) related to the first 9 eigentriples. The
 504 scale in the horizontal x-axis represents the window length ($L*15$ minutes) and the scale in
 505 vertical y-axis represents the Principal Component (PC).



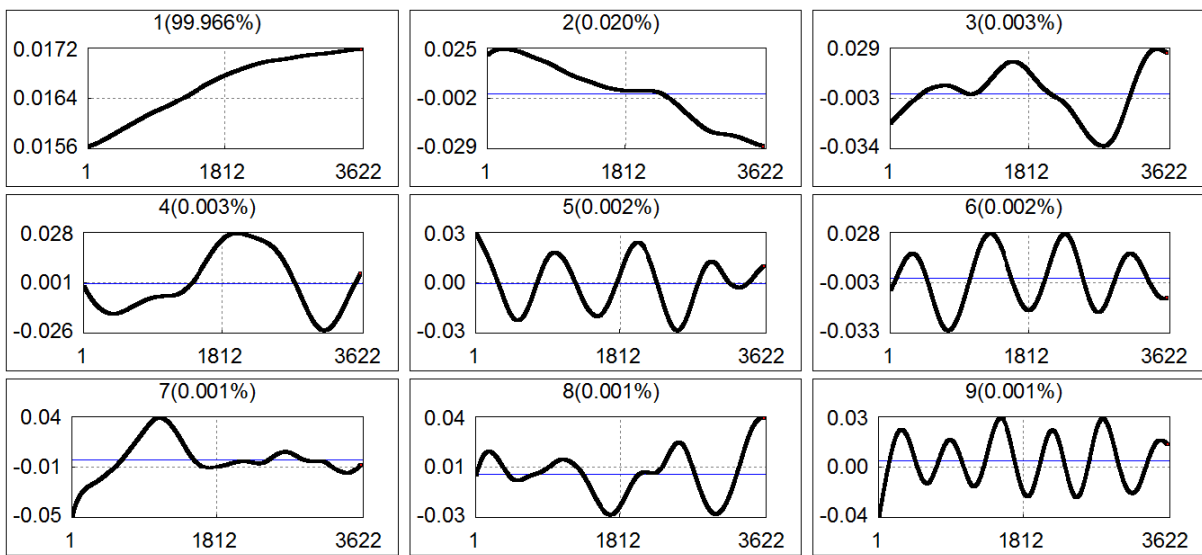
506

507 **Figure 6:** w-correlation matrix for the 9 reconstructed components of soil radon time series.

508



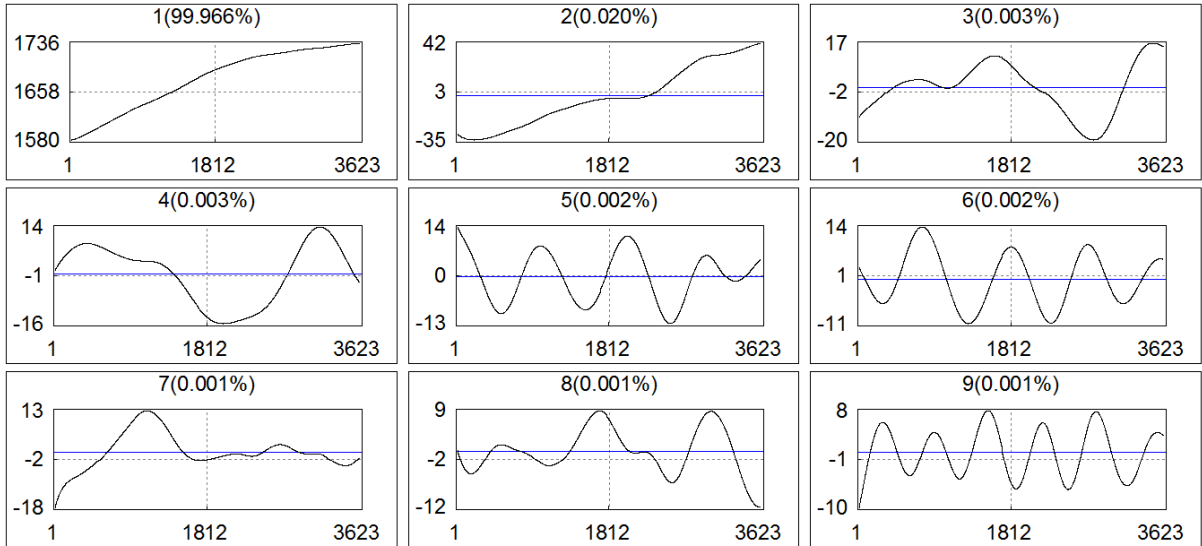
509
510 **Figure 7:** Covariance matrix of the first 9 group of soil temperature time series.



511
512 **Figure 8:** Eigenfunctions of soil temperature first 9 group. The scale in the horizontal x-axis
513 represents the window length (L *15 minutes) and the scale in the vertical y-axis represents the
514 singular eigenvectors (matrix path SVD).

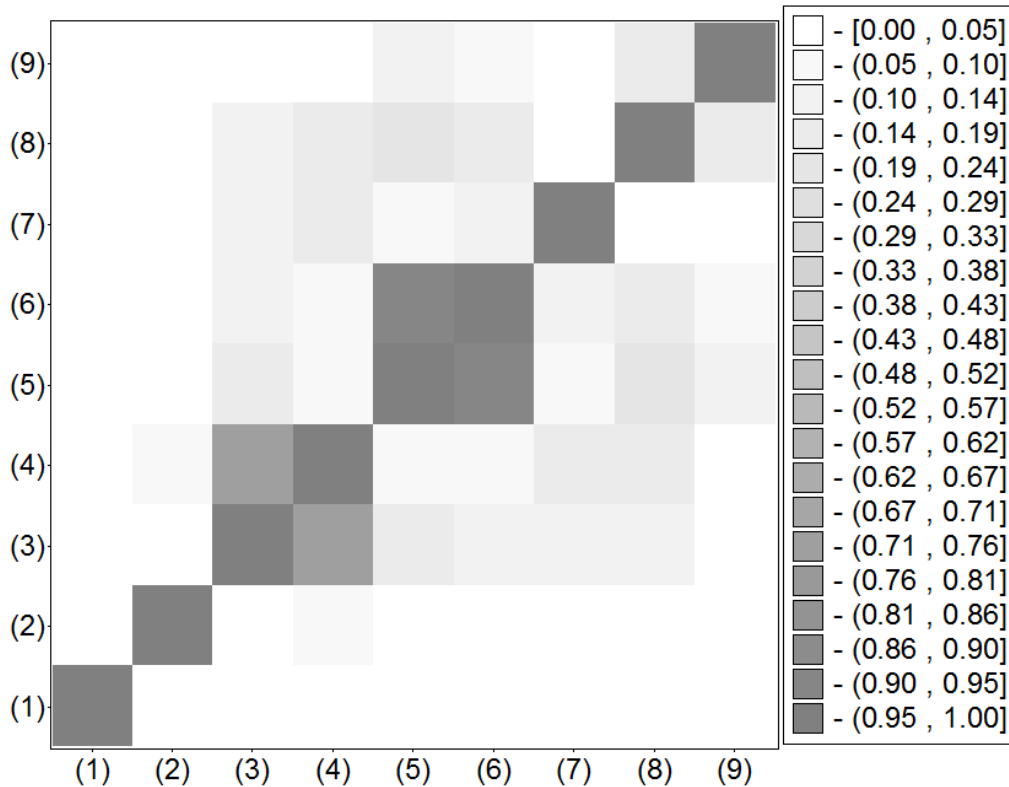
515

REVISED VERSION



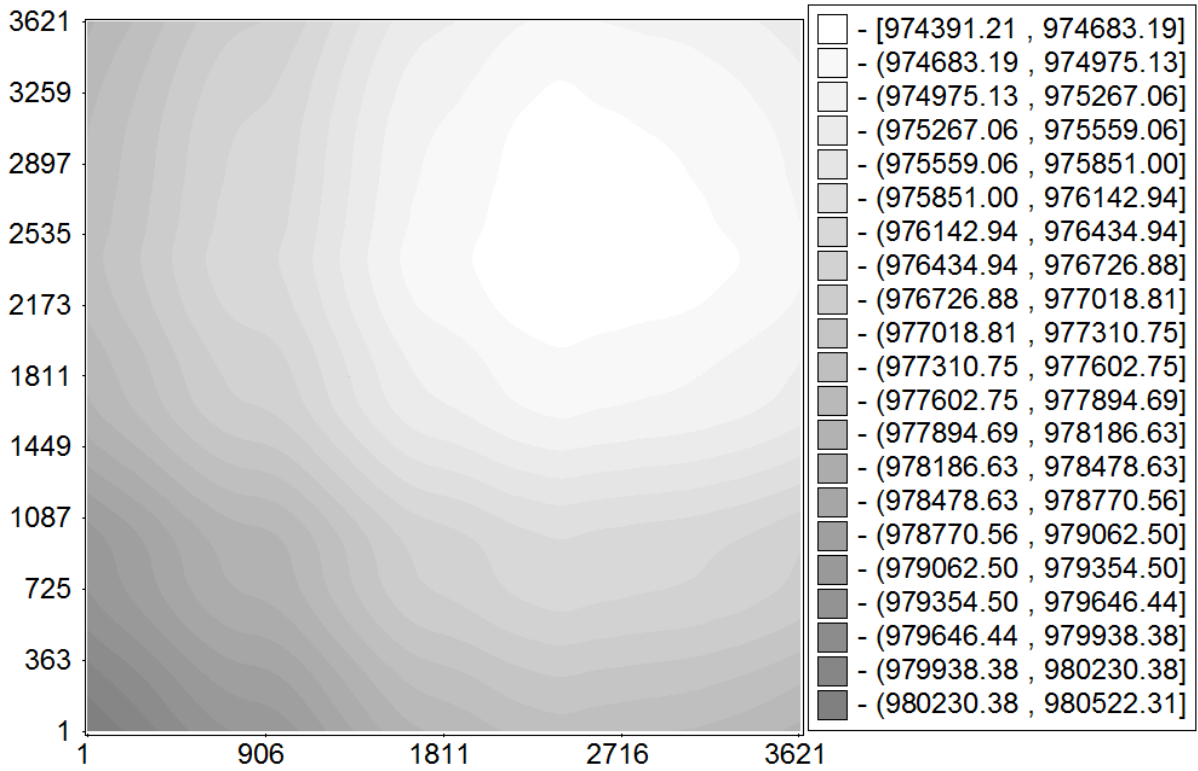
516

517 **Figure 9:** Principal Component of soil temperature related to the first 9 eigentriples. The scale
 518 in the horizontal x-axis represents the window length ($L \cdot 15$ minutes) and the scale in the
 519 vertical y-axis represents the Principal Component (PC).



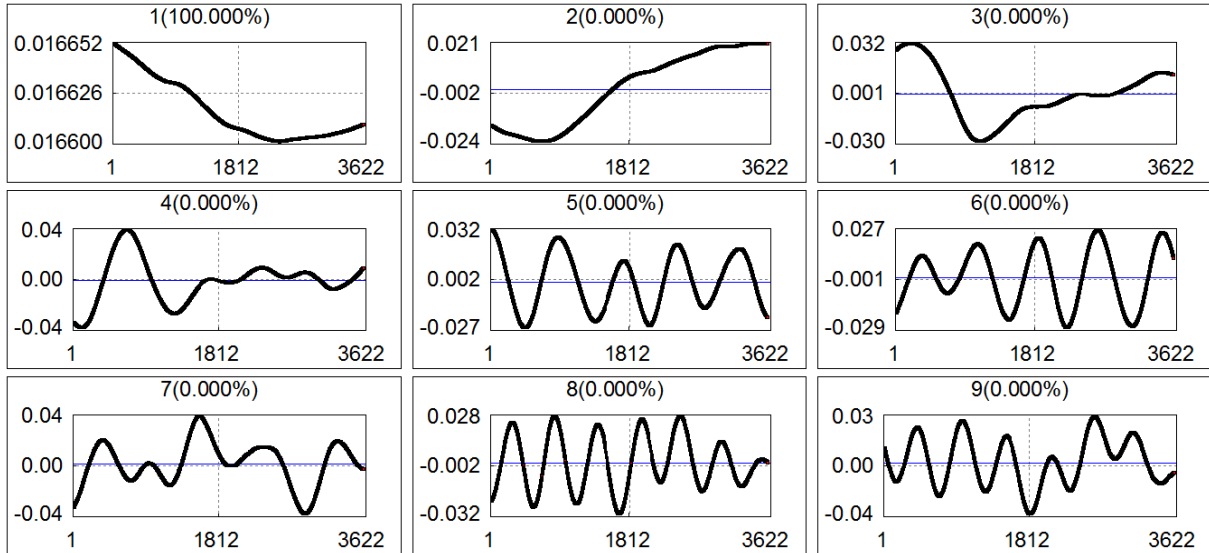
520

521 **Figure 10:** w-Correlation matrix for the 9 reconstructed components of soil temperature time
 522 series.



523

524 **Figure 11:** Covariance matrix of the first 9 group of soil pressure time series

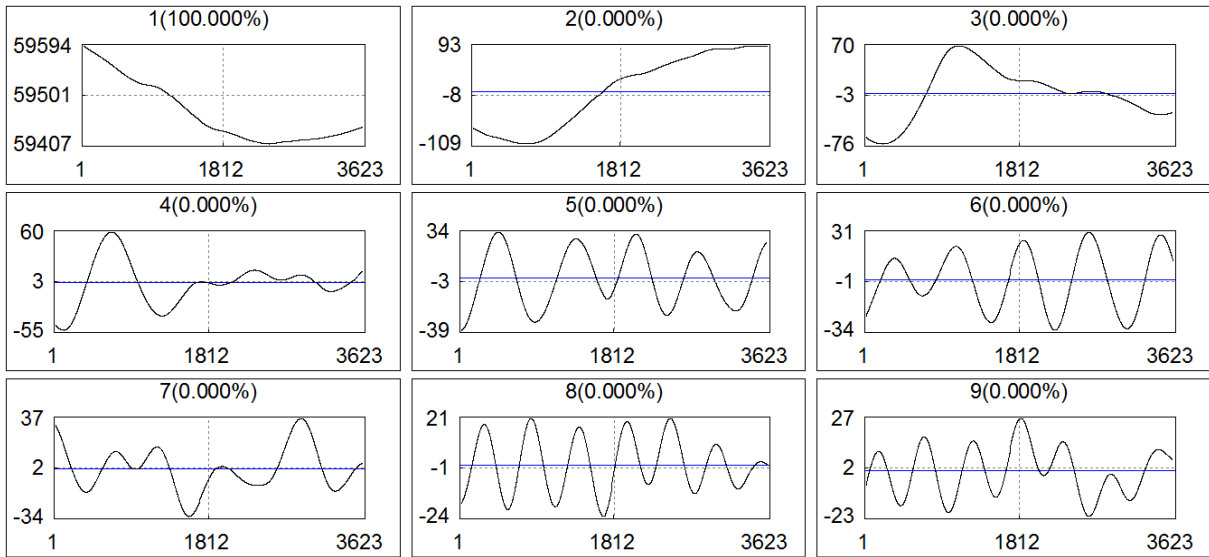


525

526 **Figure 12:** Eigenfunctions of soil pressure first 9 group. The scale in the horizontal x-axis
 527 represents the window length ($L*15$ minutes) and the scale in the vertical y-axis represents the
 528 singular eigenvectors (matrix path SVD). .

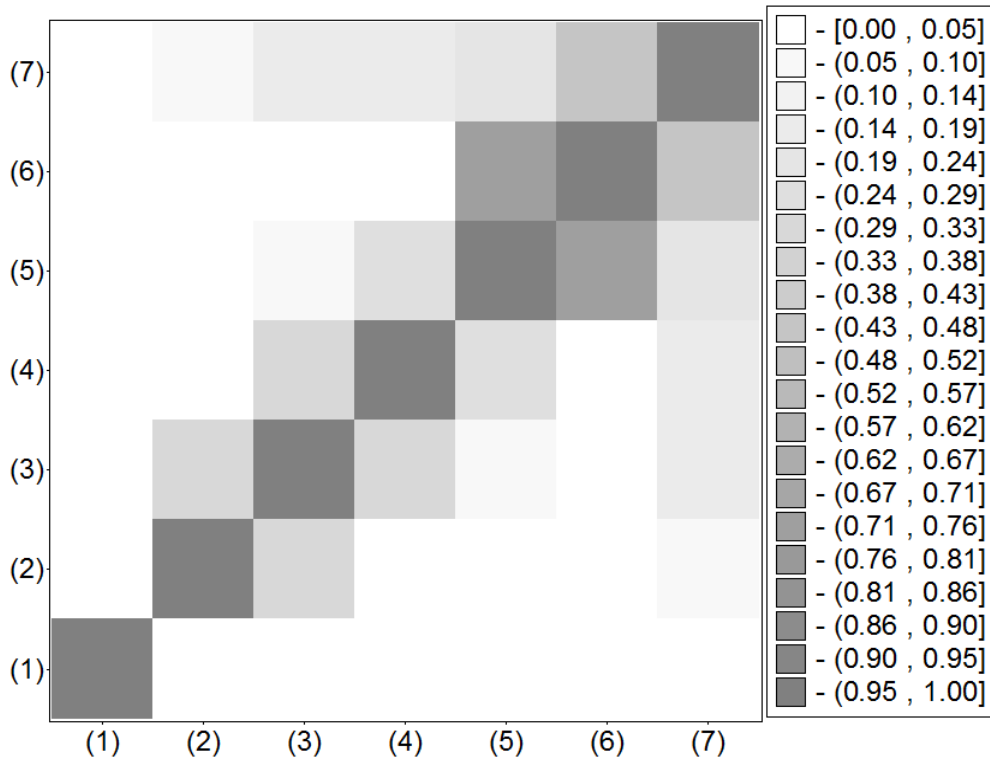
529

530



531

532 **Figure 13:** Principal Component of soil temperature related to the first 9 Eigentriples. The
 533 scale in the horizontal x-axis represents the window length ($L*15$ minutes) and scale in the
 534 vertical y-axis represents the Principal Component (PC).

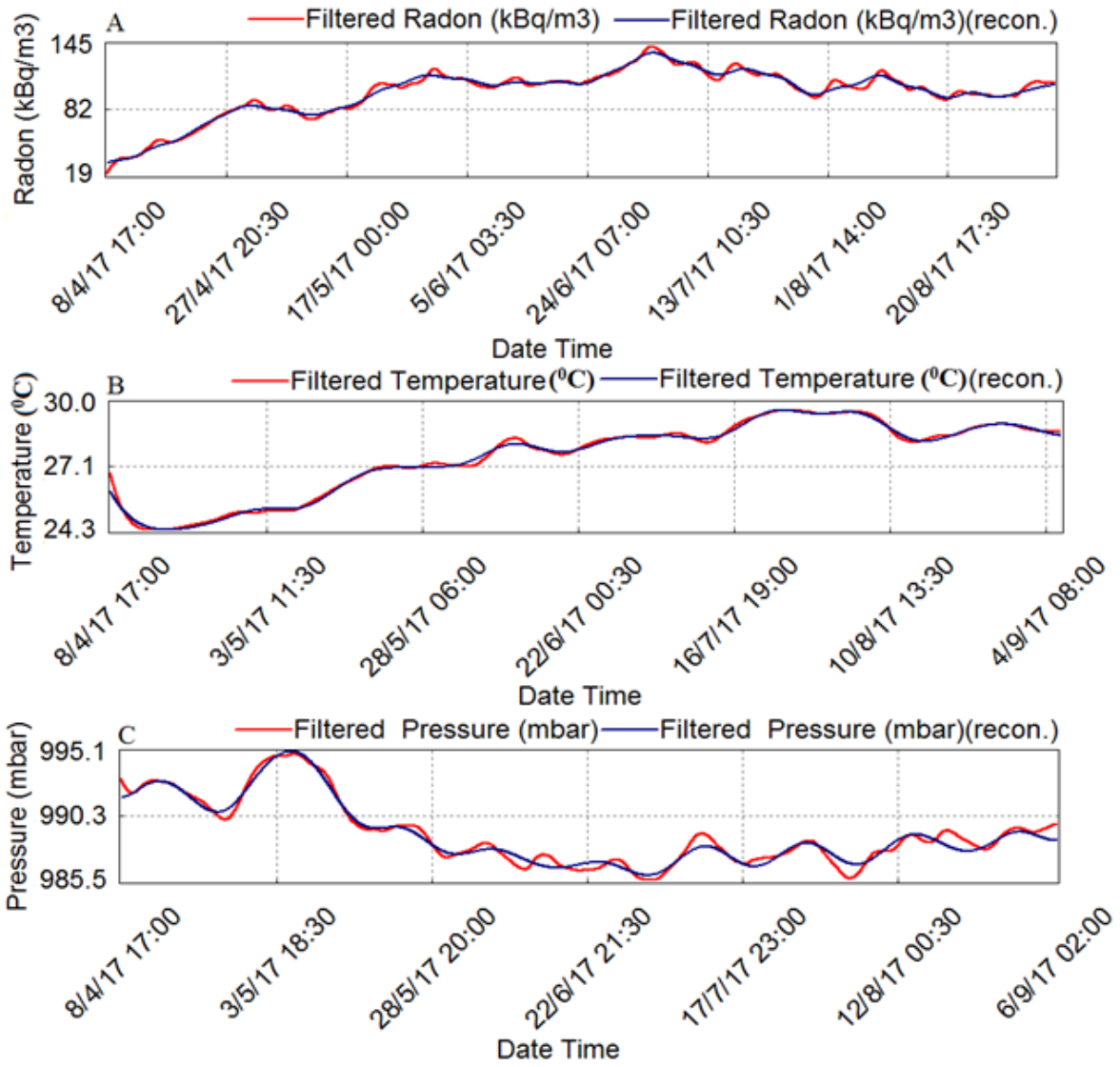


535

536 **Figure 14:** w correlation matrix for the 9 reconstructed components of soil pressure time series.

537

538



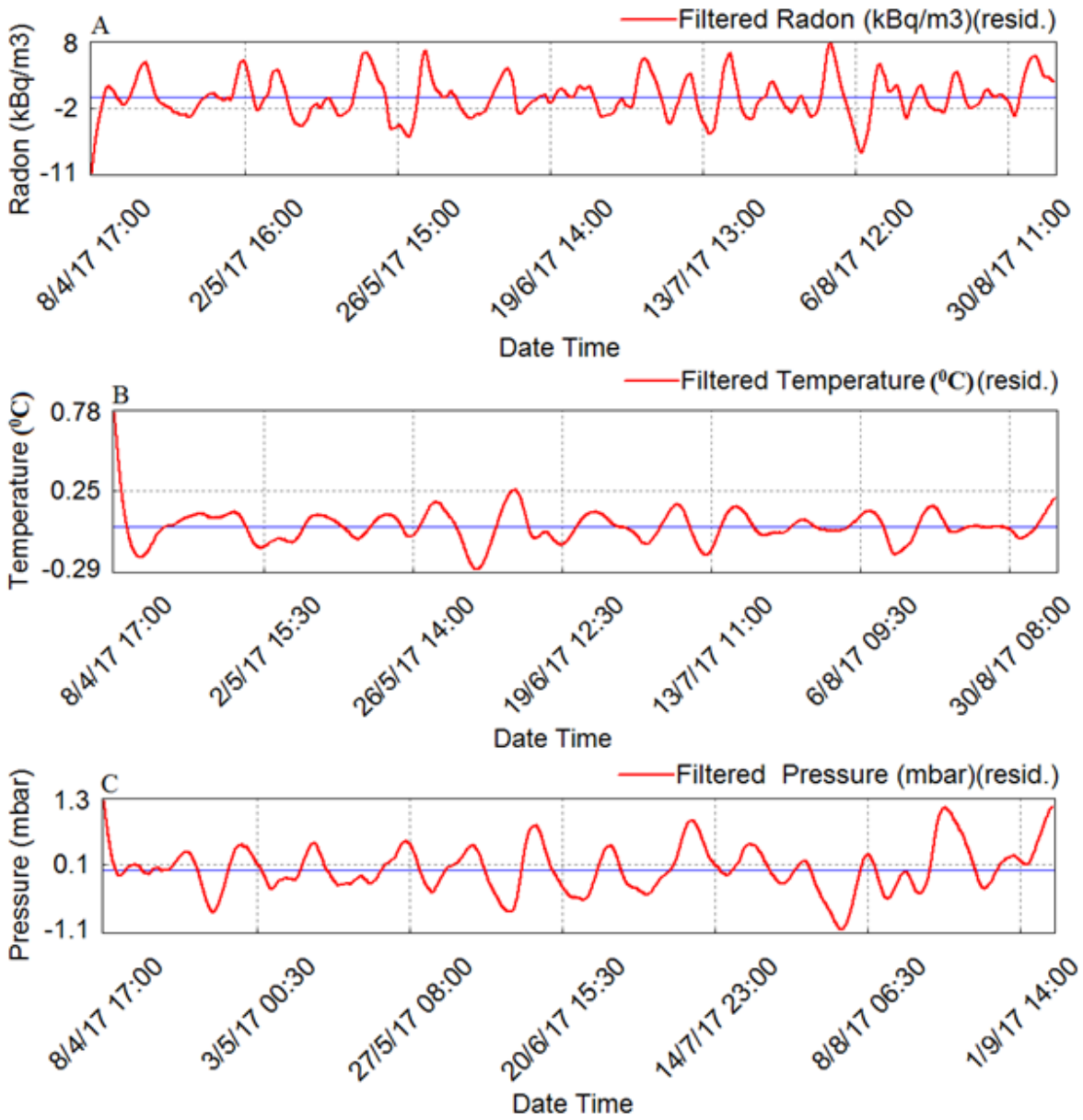
539

540 **Figure 15:** Plot showing the reconstructed time series of A) filtered soil radon, B) filtered
541 temperature and C) filtered pressure.

542

543

544



545

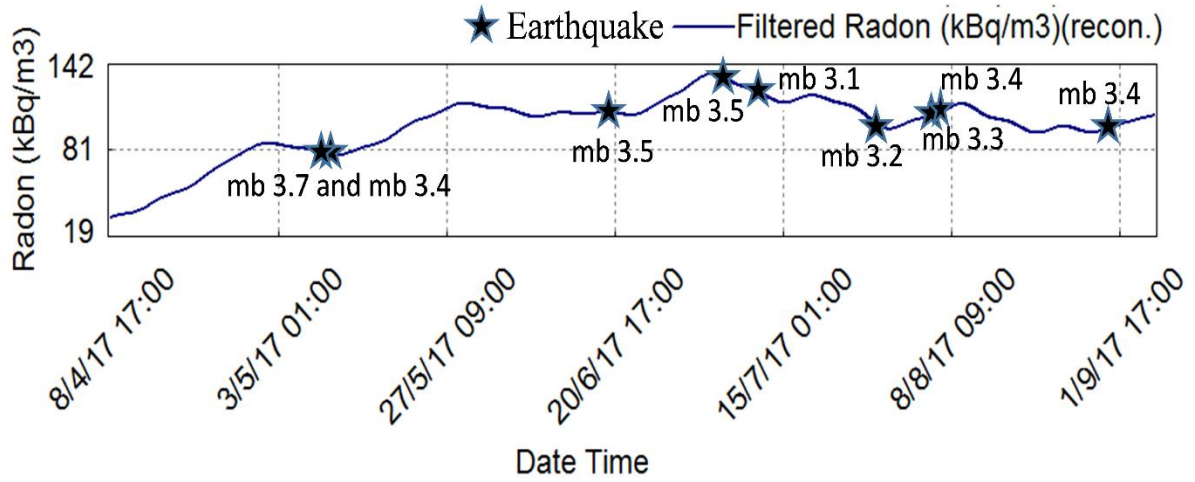
546 **Figure 16:** Residual of reconstructed time series of A) Filtered soil radon, B) temperature and

547 C) pressure respectively.

548

549

550



551

552 **Figure 17:** Plot showing the reconstructed filtered time series of soil radon emanation along
 553 with earthquake during the investigation period in the vicinity of MPGO, Tezpur (~100 km
 554 radially from MPGO) which occurred in a very short span of time.

555

556

557

558

559

560

561

562

563

564

565 **Table 1:** The average emanation of soil-gas radon and the standard deviation at MPGO from
 566 April to September, 2017.

Month (2017)	Average Rn-222 emanation (kBq /m3)	Standard Deviation (kBq /m3)
April	55.94	21.3
May	93.11	28.53
June	109.12	19.07
July	117.69	28.09
August	101.45	25.86
September	92.34	18.65

567

568

569 **Table 2:** The correlation co-efficient of soil radon gas concentration with soil pressure and
 570 temperature at OH-MPGO during year 2017.

Parameters	Average (Avg.)	Standard Deviation (Std.)	Coefficient of Variation (Std./Avg. %)	Correlation Coefficient
Radon (KBq/m³)	94.94	23.58	24.84	----
Temperature (⁰C)	28.60	0.62	2.19	0.51
Pressure (mbar)	991.03	2.48	0.25	-0.52

571

572

573

REVISED VERSION

574 **Table 3:** Hypocentral parameters of the earthquake events found to have correlation with radon
 575 anomaly.

Date of Event	UTC TIME	Lat (°N)	Long (°E)	Place	Depth (km)	Mag (m_b)	Distance from MPO (km)	Type of Anomaly (+ or -)
9/5/17	01:53:55	26.3	92.7	Assam	25	3.7	44	+
9/5/17	03:26:54	26.6	93.2	Assam	28	3.4	67	+
20/6/17	04:31:58	27.1	92.5	West Kameng, Arunachal Pradesh	10	3.5	67	+
4/7/17	10:05:47	27.0	92.1	West Kameng, Arunachal Pradesh	10	3.5	78	-
10/7/17	23:28:30	27.1	93.8	Papumpare, Arunachal Pradesh	10	3.1	78	-
25/7/17	18:28:00	26.3	93.1	Karbi Anglong, Assam	28	3.2	67	-
5/8/17	12:24:56	26.8	92.2	Darrang, Assam	10	3.3	44	+
7/8/17	11:25:07	26.3	91.7	Kamrup, Assam	10	3.4	100	+
31/8/17	17:57:26	26.6	92.7	Sonitpur Assam	10	3.4	67	+

576

577

578

579

580

581